This is a preprint that been submitted to Geophysical Research Letters, and revised based on one round of peer review at that journal, but has yet to be formally accepted for publication.

# A Multiplex Rupture Sequence under Complex Fault Network due to Preceding Earthquake Swarms during the 2024 Mw 7.5 Noto Peninsula, Japan, Earthquake

**Ryo Okuwaki[1], Yuji Yagi[1], Asuka Murakami[2], Yukitoshi Fukahata[3]**

[1]Institute of Life and Environmental Sciences, University of Tsukuba, Tsukuba, Ibaraki 305-8572, Japan

[2]Graduate School of Science and Technology, University of Tsukuba, Tsukuba, Ibaraki 305-8572, Japan

[3]Disaster Prevention Research Institute, Kyoto University, Uji, Kyoto, 611-0011, Japan

**Key Points:**

- The 2024 Mw 7.5 Noto Peninsula earthquake involves a multi-segmented rupture sequence on differently oriented faults
- A long and quiet initial rupture domain coincides with the preceding earthquake swarm region
- Fluid-induced earthquake swarms and segmented fault network control the complex earthquake rupture growth

## Abstract

A devastating earthquake with moment magnitude 7.5 occurred in the Noto Peninsula, central Japan. We estimate the rupture evolution of this earthquake from teleseismic P-wave data using the potency-density tensor inversion method, which can give spatiotemporal slip distribution including the information on fault orientations. The result shows a long and quiet initial rupture phase, which overlaps the regions of the preceding earthquake swarms and the associated aseismic deformation. The following three major rupture episodes evolve on segmented, differently oriented faults, which are bounded by the initial rupture region. The irregular initial rupture process followed by the multi-scale rupture growth are considered to be controlled by the preceding seismic and aseismic processes and the geometric complexity of fault system. Such a discrete rupture scenario, including the triggering of an isolated fault rupture, add critical inputs on the assessment of strong ground motion and associated damages for future earthquakes.

## Plain Language Summary

On 1st January 2024, a moment magnitude 7.5 earthquake occurred in the northern Noto Peninsula, Japan. The strong ground motion and tsunami associated with the earthquake caused severe damage to the buildings and infrastructures, resulting in at least 241 causalities in the affected areas as of writing this paper. The Noto Peninsula is affected by northwest-

Corresponding author: Ryo Okuwaki, rokuwaki@geol.tsukuba.ac.jp

southeast compression, and the active reverse faults are known along the northern coast of the peninsula and the offshore region. Before the 2024 earthquake, the source region has experienced long-lasting earthquake swarm activity, which is a set of seismic events without an obvious mainshock-aftershock pattern. Our seismological analysis finds that the earthquake rupture is characterized by a series of three different rupture episodes on differently oriented fault segments, following the 10-s long initial rupture episode around the hypocenter, which overlaps with the swarm region. The 2024 Noto Peninsula earthquake highlights a multi-scale rupture growth across the segmented fault network, following a very quiet initial rupture process that is controlled by the preceding earthquake swarms and the associated aseismic deformation related to the fluid injection from depth. The rupture process advances our understanding of earthquake source physics, leading to a better assessment of future earthquake hazards.

## 1 Introduction

A growing observational evidence has unveiled diverse earthquake rupture behaviors, which showcase for example, multiplex triggering ruptures (Meng et al., 2012; Hicks & Rietbrock, 2015; Fan et al., 2016; Vasyura-Bathke et al., 2024), transient rupture deceleration and acceleration (Bao et al., 2019; Ding et al., 2023), or an apparent backward rupture propagation (Hicks et al., 2020; Vallée et al., 2023). Configuration of a complex fault network can be a key driver of multi-scale cascading ruptures with alternate rupture directions (Yamashita, Yagi, & Okuwaki, 2022; Ohara et al., 2023; Okuwaki et al., 2023). Even without apparent geometric complexity of fault system, complicated bypassing or boomerang-like rupturing can be induced by inhomogeneous barriers on the fault surface due to heterogeneous fracture energy or strength (Hicks et al., 2020; Yagi et al., 2024). Complex rupture sequences on differently oriented faults can impact generating strong ground motion (e.g. Aochi & Madariaga, 2003; Chu et al., 2021; Yagi et al., 2023; Taufiqurrahman et al., 2023). Robust estimates of diverse rupture behaviors are beneficial for our better understanding of earthquake-source physics, which also adds critical inputs into better assessment of earthquake hazards, especially when it involves a complex fault network within heterogeneous media.

Noto Peninsula in central Japan (Fig. 1) is one such environment. Active faults are distributed in the off-shore region along the northern coast of the peninsula, forming a segmented fault network (AIST, 2012). The active faults are characterized by reverse faulting resulted from northwest-southeast oriented compression, which are considered to the ones re-activated under inversion tectonics from normal faulting formed at the opening event of the Japan Sea before 15–20 Ma (e.g. Sato, 1994; Okamura et al., 1995). It is not rare to have modest to large magnitude ($M$) 6 class earthquakes in this region; recent major events were the 2007 $M$ 6.9 and the 2023 $M$ 6.5 earthquakes (Japan Meteorological Agency, 2024; Hiramatsu et al., 2008; Yoshida, Uno, et al., 2023) (Fig. 1). The 2023 $M$ 6.5 event, which occurred in the northern tip of the peninsula, was preceded by the long-lived earthquake swarms from early November 2020 (Amezawa et al., 2023; Yoshida, Uno, et al., 2023; Yoshida, Uchida, et al., 2023; Kato, 2024; Shelly, 2024). Geodetic analyses suggest a series of transient aseismic to seismic deformation from deep to shallow domains, that is aseismic deformation caused by fluid spread from depths, which triggered up-dip earthquake swarm activity (Nishimura et al., 2023). Thus, the Noto Peninsula provides an intriguing environment that can cause earthquake rupture under geometrically complex fault segments and spatially heterogeneous strength fields due to existence of fluids.

On January 1st, 2024, a moment magnitude ($M_W$) 7.5 earthquake occurred in the northern Noto Peninsula, Japan (Japan Meteorological Agency, 2024) (Fig. 1). The 2024 Noto Peninsula earthquake has severely affected people and infrastructures due to strong shaking, leaving at least 241 causalities as of March 5, 2024 (Fire and Disaster Management Agency, 2024). The global centroid moment tensor (GCMT) project (Dziewonski et al., 1981; Ekström et al., 2012) finds the earthquake is characterized by reverse faulting due to northwest-southeast oriented compression. Aftershocks determined by the Japan Meteorological Agency (Japan Meteorological Agency, 2024) extend out about 150 km in the northeast-southwest direction, slightly changing the strike with a subtle S-shaped curve (Fig. 1). Dipping directions of the aftershocks are not obvious, but they roughly show a southeast-dipping in the western side of the epicenter, while northwest-dipping in the eastern side (Fig. S1). The Synthetic Aperture Radar (SAR) data (Geospatial Information Authority of Japan, 2024) shows major two patches of deformation in the western side of the epicenter, including up to around 4 m vertical displacement. Tsunami has also been recorded at the gauges along the coast (Fujii & Satake, 2024; Mizutani et al., 2024; Kutschera et al., 2024).

These early observations collectively suggest that the mainshock fault geometry is not as simple as defined by a sole rectangle plane, but has curved and/or segmented planes, which stimulates us to know how the earthquake rupture is related to the geometric complexity of faults. It is inherently challenging to understand a causal relationship between rupture evolution and geometric feature of faults in an observational basis, because an inappropriate assumption of fault geometry, which is one of the major sources of modeling errors, can easily bias the solution, making it difficult for robust interpretation of source processes (e.g. Ragon et al., 2018; Shimizu et al., 2020). Here for the analysis of the 2024 Noto Peninsula earthquake, we apply a recently developed potency-density tensor inversion (PDTI) method, which can flexibly estimate rupture evolution without strong assumption on fault geometry (Yagi & Fukahata, 2011; Shimizu et al., 2020; Yamashita, Yagi, Okuwaki, Shimizu, et al., 2022). We discuss a multiplex rupture sequence across the segmented fault network and its relation to the preceding earthquake swarm, which control the nucleation process and irregular rupture behavior of the 2024 Noto Peninsula earthquake.

## 2 Data and Methods

Inappropriate assumption of fault geometry is one of the major sources of modeling errors in a finite-fault inversion (Ragon et al., 2018; Shimizu et al., 2020; Dutta et al., 2021). One can assume a realistic fault geometry by prescribing a single or multi finite-fault planes guided by active faults, slab geometry models, or aftershock distributions, which however is not necessarily the true fault geometry that hosts the co-seismic rupture of interests. Especially the conventional finite-fault inversion method requires to strictly force the fault slip vectors to span the prescribed model surface, which is a strong constraint that may induce modeling errors when the assumption of fault geometry is inappropriate, leading to bias in both the modeling and interpretation. A recently developed PDTI method (Shimizu et al., 2020) solves for the potency-rate density tensor distribution by alternatively representing a fault slip as a composite of five-basis moment tensors (e.g. Kikuchi & Kanamori, 1991), which is independent of the prescribed model fault plane and thus enables us to simultaneously estimate both the rupture evolution and fault geometry. The flexible approach has helped avoid modeling bias, and lead to robust modeling of the earthquake source processes, which has been proven efficient to model the diverse rupture processes over variety of tectonic environments or unknown fault configurations (e.g. Shimizu et al., 2020; Tadapansawut et al., 2021; Okuwaki & Fan, 2022; Yagi et al., 2023; Ohara et al., 2024).

For the 2024 Noto Peninsula earthquake, both the active faults and the aftershocks show spatial changes of fault strike and dipping orientation (Figs. 1 and S1). Such features motivate us to use the PDTI method to analyze the source process of the 2024 Noto Peninsula earthquake. We echo here that our PDTI approach does not need a strict assumption about the fault geometry; the adopted model space geometry (model fault) does not necessarily coincide with the actual fault geometry. Such a flexible representation of earthquake sources can be made by projection of intrinsically volumetric distribution of potency-rate density tensors onto a 2-D model faults (Shimizu et al., 2020). Teleseismic body waves have rich information about source evolution, including the variation of focal mechanisms (Kikuchi & Kanamori, 1991; Shimizu et al., 2020, 2021), whilst the spatial resolution is relatively low compared to other near-field datasets (e.g. SAR). The PDTI method using the teleseismic body waves is not very sensitive to the error of source location, which is in turn a theoretical ground that our PDTI approach does not require strict assumption of fault geometry. However still, the dipping angle of model geometry may affect the final solution, as the Green's function changes in depth. Because of that, the horizontal location of slip can vary according to the horizontal location and the dip direction of model faults. In this study, we build source models upon alternative two model faults (Fig. S1): (1) a twin model fault with a composite of southeast and northwest dipping planes (strike/dip: 55°/35° and 225°/35°) and (2) a single model fault with a southeast dipping plane (55°/35°). For the twin model fault, fault lengths are 95 km in the western section and 55 km in the eastern section. For the single model fault, the fault length is 150 km. For both the models, a fault width is 35 km, and the model faults are discretized into 5 km × 5 km subfaults both along the strike and dip directions. In the following, we primarily focus on the result of the twin model fault, but we will discuss in the later section how this model setup may affect the solution and our interpretation of the source process of the 2024 Noto Peninsula earthquake.

We adopt a hypothetical model rupture front that defines a timing of rupture initiation at each source element, propagating at 3.9 km/s based on the $S$-wave velocity around the source region (Table S1), which is fast enough to allow various rupture scenarios. We represent a slip time function at each source element by a series of linear B splines at 0.6-s interval. We set a duration of the slip time function at each source element from the hypothetical rupture initiation to the rupture termination, which is set 45 seconds later from the start of this earthquake. Such a wide model space enables us to flexibly represent potentially irregular rupture or slip behaviors, including the multiple peaks of slip, reverse migration of rupture front or re-rupture at a certain source point.

We use a vertical component of the teleseismic waveforms at 32 globally operated broadband stations via the SAGE Data Management Center (Fig. 1). The data are selected based on clear *P*-wave arrivals that can be reliably picked and on a good azimuthal coverage (e.g. Okuwaki et al., 2016). The data are then resampled at 0.6 s interval after removing instrumental responses, and converted into velocity. Green's functions are calculated based on the method of Kikuchi and Kanamori (1991). The structural velocity model of the ak135 (Kennett et al., 1995) is adopted for near the source region to calculate the Green's functions. The selection of the velocity model is evaluated by adopting an alternative model of the CRUST 1.0 (Laske et al., 2013) (Table S2); we find that the selection of the velocity model does not significantly affect the solution (Fig. S2). The JMA registers the information of the mainshock as the JMA magnitude ($M_{\mathrm{JMA}}$) 7.6 at 37.496°N, 137.271°E at 2024-01-01 07:10:22 (UTC), but preceding that event, they also register the $M_{\mathrm{JMA}}$ 5.9 foreshock at 37.508°N, 137.230°E at 2024-01-01 07:10:09 (UTC) (Japan Meteorological Agency, 2024). After inspecting the teleseismic dataset, clearer onsets of *P* waves can rather be identified for the signals associated with the preceding event. Thus, we regard both the $M_{\mathrm{JMA}}$ 5.9 and 7.6 events as a series of the mainshock sequence, and an initial rupture point (hypocenter) is adopted as 37.508°N, 137.230°E, and 12 km depth for our modeling of the 2024 Noto Peninsula earthquake.

## 3 Results

As shown in Figs. 2–4, the source model built by the PDTI for the 2024 Noto Peninsula earthquake shows a series of discrete rupture episodes: E1, E2, and E3, which follows a long (about 10 s) and quiet initial rupture episode E0 around the hypocenter. The timing and location of these rupture episodes can be referred to Fig. 4. The total seismic moment is $2.5\times10^{20}$ N m ($M_{\mathrm{W}}$ 7.5). The general faulting mechanism extracted from the space-time integration of all the potency-rate density tensors is characterized by reverse faulting with northwest-southeast compression (Fig. 1), but involving considerable changes of fault geometry in space and time, which will be described below. In this section, we primarily focus on the result built upon the twin model fault. We emphasize here in advance that both the models of the single and twin model faults share common features of rupture evolution and fault geometry with comparable data fits (Figs. S7 and S8). The discrepancy of these models that may affect interpretation of the results will be discussed in the Discussion section.

### 3.1 A quiet initial rupture episode: E0

During the first 10 s after the origin time, there is a minor initial rupture episode around the hypocenter, which corresponds to 1% of the total seismic moment ($M_{\mathrm{W}}$ 6.3). The best-fitting double couple solution extracted from the resultant potency-rate density of this episode shows reverse faulting with the strike of 68° at the maximum location of the potency rate. The rupture direction is not clearly inferred, but mainly propagates toward west from the hypocenter (Fig. 2).

### 3.2 A minor rupture episode: E1

From 10 s after the origin time, a higher potency-rate event than the E0 begins around from 0 km to 40 km west from the hypocenter; this episode continues until 24 s. The strike angle extracted from the potency-rate density tensors of this episode is 55° at the maximum location of the potency rate, which is the same as the strike angle (55°) of the corresponding section of the model fault (Figs. 3 and 4). The E1 ruptures mostly a shallow domain (< 15 km).

### 3.3 A major rupture episode in the western section: E2

In the western section of the model fault, a major event occurs from 25 s to 36 s after the origin time. It extends from around 0 km to 65 km west of the hypocenter. The strike angles during the E2 rotate counter-clockwise from those in E1 toward the north-south direction with a range of 21° to 48° (Fig. 4). The strike at the maximum location of the potency rate is 37°. This E2 event ruptures up to 20 km in the depth, which is deeper than the E1.

### 3.4 A major rupture episode in the eastern section: E3

At almost the same timing as E2, another major rupture episode E3 occurs in the eastern section during 26–34 s. It extends from 10 to 60 km east of the hypocenter. The strike angles during the E3 also rotate counter-clockwise from those in E1 with a range from 215° to 224°, which are more aligned than during the E2 (Fig. 4); the strike at the maximum location of the potency rate is 215°. Note that for E3, the strike angle is selected from the ones of the double-couple solution that is close to the northwest-dipping model plane. As discussed in the later section, the highest potency rate is generally obtained in the shallow part for both the twin and single fault models; because of the alternate dipping sense of the model faults, the twin fault model finds the highest potency rate close to the southern side of the model fault, whilst the single model finds it to the northern side of the model fault (Figs. 4, S4 and S6). The rupture becomes suddenly faint after 34 s, with a minor moment-rate release during 38 to 42 s.

## 4 Discussion

### 4.1 Discrete rupture episodes robustly estimated against model setups

As described in the preceding section, the source process of the 2024 Noto Peninsula earthquake can be characterized by spatiotemporally segmented multiple rupture episodes. Our model finds the rupture episodes in the western (E1, E2) and eastern (E3) model domains are separated by the hypocenter region, which only hosts the minor initial rupture episode E0. In order to evaluate if such a discrete nature of rupture process is artificially made by the segmented domains designed for the twin model fault, we perform the same inversion procedure, but using an alternative model fault geometry composed of a single southeast-dipping plane without imposing any prescribed segments (Figs. S3–S5). Even in this case, the subtle initial rupture episode (E0) is robustly estimated, which is followed by the E1 and E2 rupture episodes in the western side. The near-field records from the local stations show the relatively larger amplitude at the station in the western side of the epicenter (Fig. S11), which may indicate a directivity of rupture during the first 10 s and be consistent with the westward rupture direction of the E0. The E3 is also found in the eastern section across the hypocenter. The strike changes among the rupture episodes are similar to what has been estimated for the twin fault model; the strike orientations of both E2 and E3 rotate counter-clockwise from the reference model strike (55°) (Fig. 4). These common features retrieved from the two different model setups suggest that the segmented rupture episodes separated by the hypocenter are robust features of the 2024 Noto Peninsula earthquake.

A significant difference of the results among the two models is their slip locations in the eastern section. For the twin fault model adopting the northwest-dipping segment in the east, the highest potency rate locates in the south-eastern side of the eastern fault, whilst the single fault model finds the highest potency rate in the north-western side (Fig. S6). Here, it should be noted that our modeling approach leaves an ambiguity of the dipping sense, mostly due to the lower spatial resolution of the teleseismic data, compared to those of the near-field data sets. Absolute slip locations will still need to be further evaluated with the other data sets that have enough sensitivity to the slip location, such as tsunami data, although this is beyond the primary scope of this study. Our approach is advantageous to robustly estimate rupture evolution and the fault geometry changes against a selection of model setup. Also this exercise adopting conjugate dipping planes suggest that our modeling approach can constrain the rupture depth, which shows concentration on the shallower domain for both the model faults.

### 4.2 Control of rupture behavior due to preceding earthquake swarms

Our source model shows the initial rupture episode (E0) is quiet and lasts 10 s before the main rupture initiates. As mentioned in the Data and Methods section, we regard the preceding $M_{\mathrm{JMA}}$ 5.9 and the subsequent $M_{\mathrm{JMA}}$ 7.6 events as one continuous earthquake. The near-field strong motion records show the $M_{\mathrm{JMA}}$ 5.9 event had an unusually long duration, when compared with other similar-sized events, and did not terminate before the $M_{\mathrm{JMA}}$ 7.6 event initiated (Fig. S11). An irregular initial rupture phase has been observed for other earthquakes (e.g. Ellsworth & Beroza, 1995; Abercrombie & Mori, 1994), although the 10-s duration of our E0 episode is longer than most cases documented in the literature. One exception is the 2014 $M_{\mathrm{W}}$ 8.1 Iquique, Chile, earthquake, which has a long (20 s) initial rupture phase (e.g. Yagi et al., 2014), and was preceded by 2-weeks long swarm-like foreshock activity (e.g. Ruiz et al., 2014; Kato & Nakagawa, 2014). These observations then raise the question of what environment fosters the development of such rupture behavior observed for the 2024 Noto Peninsula earthquake.

The northern tip of the Noto Peninsula near the hypocenter of the 2024 Noto Peninsula earthquake has experienced long-lived earthquake swarm activity since early November 2020, which seemingly ended up by the adjacent $M$ 6.5 earthquake on May 5, 2023 (Amezawa et al., 2023; Kato, 2024) (Figs. 1 and S9). Geodetic studies find aseismic crustal deformation accompanies the swarm activity, suggesting upwelling fluid migration from around 16 km depth to the shallow permeable fault zone, which triggers a series of diffusive aseismic processes to seismic deformation (Nishimura et al., 2023). The E0 domain overlaps the earthquake swarm region, and the eastern edge of E1 coincides with the western edge of the swarm region (Figs. 3 and 4). It is likely that the E0 domain has experienced strain release preceding the mainshock due to the fluid-induced earthquake swarms and the associated aseismic deformation, which has left an unfavorable environment for spontaneous fast rupture with large stress drop. Such a development prior to the mainshock is considered to be the cause of the long-lasting initial rupture phase of E0. Earthquake-swarm activity has often been interpreted to be associated with aseismic slip and/or fluid migration (e.g. Vidale & Shearer, 2006; Shelly et al., 2016; Fukuda, 2018; Ross et al., 2020; Nishikawa et al., 2021; Im & Avouac, 2023), which has been evaluated with numerical simulations under variable physical conditions (e.g. Zhu et al., 2020; Dublanchet & De Barros, 2021; Wang & Barbot, 2023). For example, the model incorporating permeability changes predicts fluid-driven aseismic slip and swarm seismicity, together with fluid pressurization ascending through the seismogenic zone, which can eventually lead to a large earthquake (Zhu et al., 2020). Here the 2024 Noto Peninsula earthquake should provide an additional observational evidence that the co-seismic rupture process itself is also controlled by the preceding fluid-induced swarms, which contributes to the irregular initial rupture phase and the following multiplex rupture episodes across the swarm region (Figs. 2–4).

### 4.3 Triggering of segmented fault ruptures

We observe changes of strike orientations among the rupture episodes: relatively east-west orientations for the E1 in the central section and relatively north-south orientations for the E2 and E3 in the western and eastern sections. Such changes of strike are robustly retrieved even when adopting the different model fault geometry (Fig. 4); in addition, the changes of strike are also consistent with the aftershock distribution (Japan Meteorological Agency, 2024) and the surface displacement pattern observed in the inland by SAR (Geospatial Information Authority of Japan, 2024). The distinct features of strike orientations suggest that E1 and E2 ruptures the differently oriented fault segments, which evolve from the smaller scale E1 to the larger scale E2. Such a multi-scale rupture growth controlled by geometric features of the fault system is similarly observed during the 2023 Türkiye and Syria earthquake doublet (e.g. Okuwaki et al., 2023). We note that the duration of the western rupture (E1 + E2) is longer than that for the eastern rupture (E3) (Fig. 2b). The strike orientations in the western section displays a wider range of variability than in the eastern section (Figs. 4 and S10). Although for convenience we narrate our results by defining rupture episodes (e.g. E2), given the considerable variability of the fault geometry seen during E2, the E2 domain is not necessarily a single fault, but more likely to be multiple faults that take a longer time to be ruptured, which may be related to the complex aftershock distribution in the western side of the peninsula (Fig. 1).

The E3 rupture is isolated from the other episodes, and a rupturing path either from the hypocenter or other episodes is not obvious from our solution. Although it is generally difficult to rigorously estimate rupture speed from our solution due to the limited spatial resolution and smoothing effects, we note an apparent migration speed from E1 to E3 is roughly estimated at ∼3.4 km/s that is close to the $S$-wave speed around the source region (e.g. Table S1). The distant rupture episodes such as E1 possibly contribute to dynamic disturbances on the E3 domain and resultant rupture. As discussed in the previous subsection, the absolute location of slip and dipping direction for E3 are difficult to be uniquely determined solely by our modeling using the teleseismic data, but the northwest-dipping E3 rupture found on the twin fault model likely corresponds to one of the potential tsunami source faults recognized by the Ministry of Land, Infrastructure, Transport and Tourism (MLIT) and Japan Sea Earthquake and Tsunami Research Project before the 2024 Noto earthquake (Ministry of Land, Infrastructure, Transport and Tourism, Japan, 2014). So far, such a tsunami scenario fault has been proposed to be ruptured individually, and a triggering or simultaneous rupture along with other adjacent scenario faults with considerably different fault geometry were not specifically supposed. However, multiplex rupturing across a complex fault network or segmented multi-fault triggering has been reported for earthquakes in variable tectonic environments (e.g. Kuge et al., 1996; Satriano et al., 2012; Fan et al., 2017; Nissen et al., 2016; Hamling et al., 2017; Lay et al., 2018; Yamashita, Yagi, & Okuwaki, 2022; Vasyura-Bathke et al., 2024), which results in diverse rupture behaviors, including the rupture of faults with conjugate dip directions and the apparent backward rupture propagation.

As shown in the Results section, the E2 and E3 occur almost simultaneously, but separated by the preceding earthquake swarm region around the hypocenter. This complicates the apparent rupture directions of the 2024 Noto earthquake; that is, the rupture firstly propagates toward west from the hypocenter, then, it apparently goes toward both west and east of the hypocenter, resulting in the separated E2 and E3 with a change of the dip direction across the hypocenter. The regions of the preceding earthquake swarm and the 2023 $M$ 6.5 source area around the 2024 hypocenter did not completely work as the barriers that stop the 2024 ruptures. This may add critical inputs when considering earthquake hazards in a context of short-term assessment after a series of notable events (e.g. geodetically detected aseismic deformation, intense earthquake swarms, and a major earthquake). The 2024 Noto Peninsula earthquake suggests the triggering of segmented fault ruptures with an opposite dip direction. It would be essentially important to comprehensively consider interaction with preceding seismic or geodetic activities when assessing future earthquake hazards.

## Conclusions

We find a series of discrete rupture episodes on the differently oriented fault segments for the 2024 Noto Peninsula earthquake. The 10-s long quiet initial rupture domain overlaps the preceding earthquake swarm region, which hosts the irregular nucleation process that leads to the following dynamic instabilities of the major ruptures. The multi-scale rupture growth are controlled by the complex fault network and the heterogeneous source environment that is highlighted by the swarm activity and the associated aseismic deformation. A possibility of co-ruptures of the segmented faults or triggering of isolated fault rupture with different fault orientations add critical inputs into better assessment of future earthquake hazards.

## Open Research

Materials in this paper are archived at https://doi.org/10.5281/zenodo.10812186. All seismic data were downloaded through the EarthScope Consortium Wilber 3 system (https://ds.iris.edu/wilber3/), including the following seismic networks: (1) the BK (BDSN; Northern California Earthquake Data Center, 2014); (2) the G (GEOSCOPE; Institut De Physique Du Globe De Paris (IPGP) & Ecole Et Observatoire Des Sciences De La Terre De Strasbourg (EOST), 1982); (3) the GE (GEOFON; GEOFON Data Centre, 1993); (4) the IC (NCDSN; Albuquerque Seismological Laboratory (ASL)/USGS, 1992); (5) the IU (GSN - IRIS/USGS; Albuquerque Seismological Laboratory/USGS, 2014); (6) the MN (MedNet; MedNet Project Partner Institutions, 1990); and (7) the PS (ERI/STA; University of Tokyo, Earthquake Research Institute (Todai, ERI), Japan, 1989). The strong-motion seismographs from the NIED K-NET and KiK-net (National Research Institute for Earth Science and Disaster Resilience, 2019b) was accessed through the unified Website for K-NET and KiK-net (https://www.kyoshin.bosai.go.jp/). We used Cartopy (Met Office, 2015; Elson et al., 2022), ObsPy (Beyreuther et al., 2010), Pyrocko (Heimann et al., 2017), matplotlib (Hunter, 2007), Generic Mapping Tools (Wessel et al., 2019), FPSPACK (Gasperini & Vannucci, 2003) and Scientific colour maps (Crameri, 2018; Crameri et al., 2020) for generating figures.

## Acknowledgments

We acknowledge the editor Germán Prieto, the associate editor, the reviewer Zachary Ross, and the anonymous reviewer for their thorough evaluations and constructive feedback, which have led to improvements of the manuscript. The facilities of EarthScope Consortium were used for access to waveforms, related metadata, and/or derived products used in this study. This work was supported by JSPS Grant-in-Aid for Scientific Research (C) 19K04030 and 22K03751, and JSPS Grant-in-Aid for Transformative Research Areas (A) "Science of Slow-to-Fast Earthquakes" 24H01020.

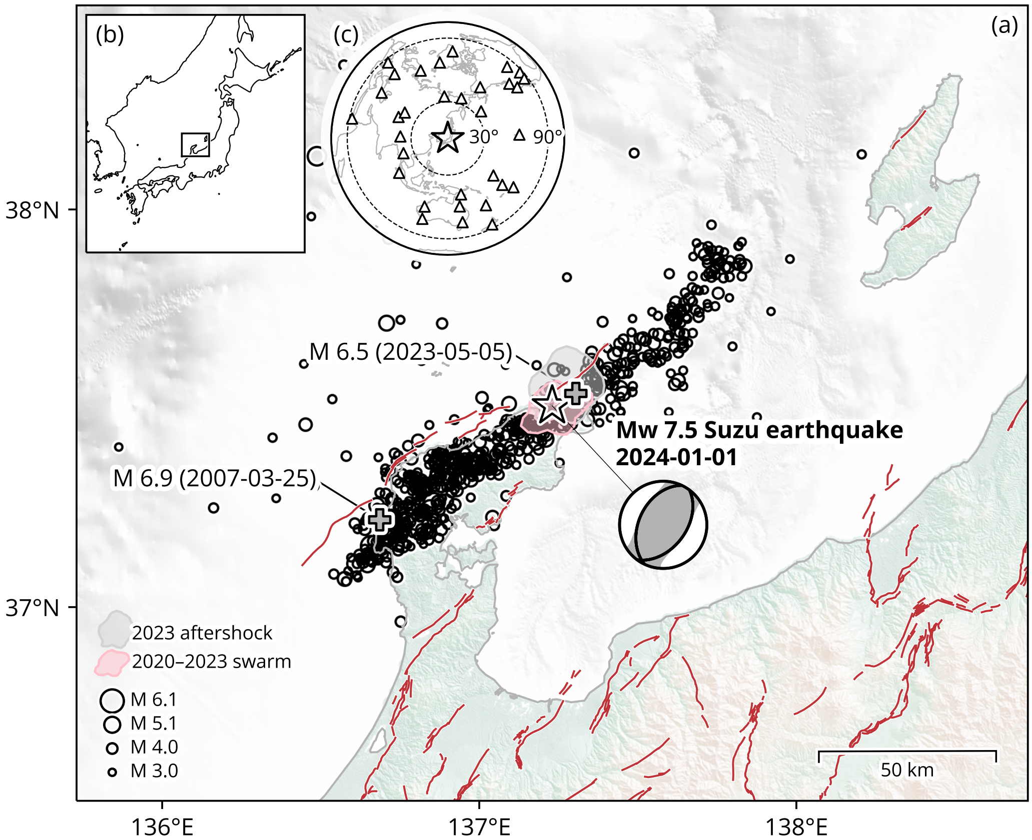


**Figure 1.** Summary of the study region of the 2024 Noto Peninsula earthquake. (a) The star denotes the epicenter. The beachball shows the estimated total moment tensor obtained by the integration of all the potency-rate density tensors. The black circles show the 24-hour aftershocks (Japan Meteorological Agency, 2024). The cross markers show the past major events. The shaded area show the regions of the 2020–2023 earthquake swarms (pink) and the 1-week aftershocks of the 2023 $M$ 6.5 earthquake (gray) based on the Gaussian kernel-density estimates (> 5% of the normalized density). The red lines are the active faults (AIST, 2012). The topography is from SRTMGL1 tiles (NASA JPL, 2013). (b) The regional map of the study region. The rectangle shows the area of Fig. 1a. (c) The station distribution (triangles) used for the analysis. The star denotes the epicenter. The dashed circles show the epicentral distances.

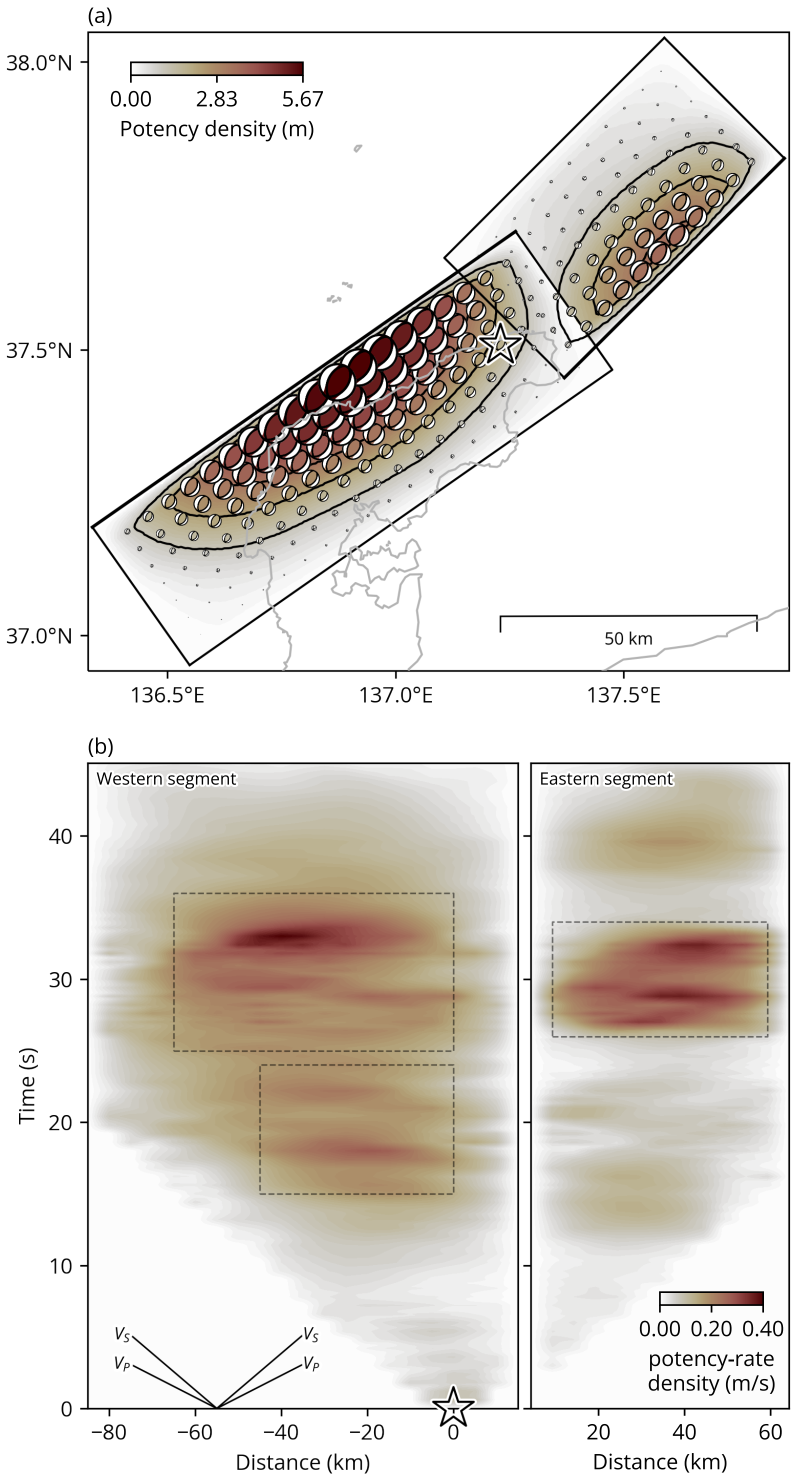


**Figure 2.** (a) The potency density tensor distribution, calculated by the integration of the potency-rate density tensors with respect to time. The star shows the hypocenter, which gives the initial rupture point. The rectangle outlines the regions of model faults. The thick black lines represent the top of the model faults. The black contour outlines potency every 1.1 m. (b) Potency-rate density evolution projected along the line of each model strike. The star represents the initial rupture point. The dashed rectangles highlight the notable rupture domains that are displayed in Figs. 3 and 4. The lines of $V_P$ and $V_S$ show the $P$ and $S$ wave speeds from the near-source structural model (Table S1).

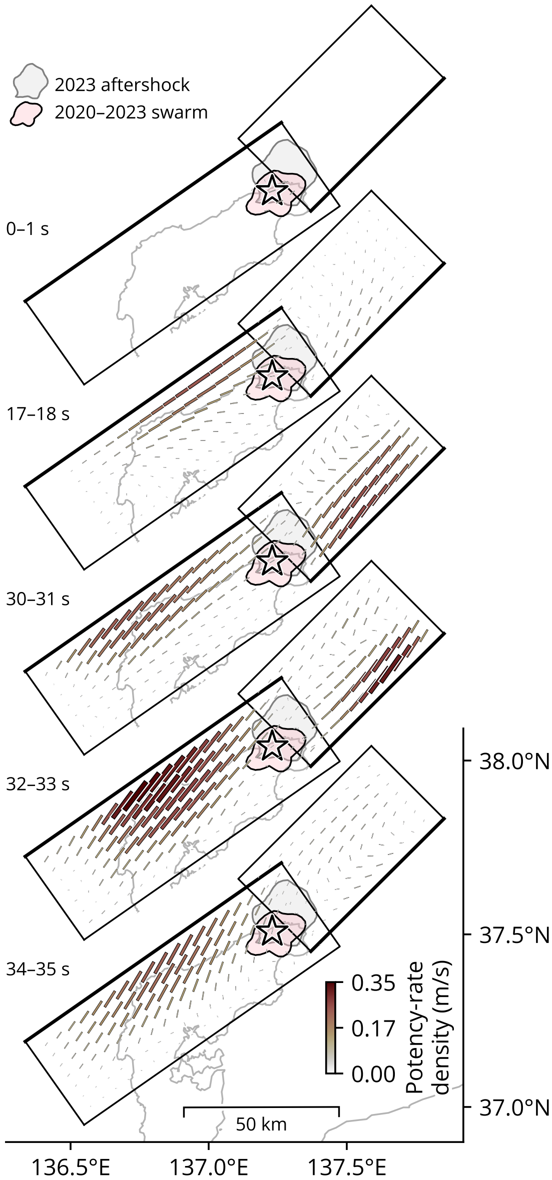


**Figure 3.** Selected snapshots of the strike orientations, extracted from the corresponding potency-rate density tensors. The bar represents the strike orientation, which is one of the two possible nodal planes of the best-fitting double couple solution that minimizes the inner product of fault-normal vectors of the candidate plane and the corresponding model plane. The bar length is scaled with the potency rate. The full snapshots of the potency-rate density tensor distribution can be seen in Movie S1.

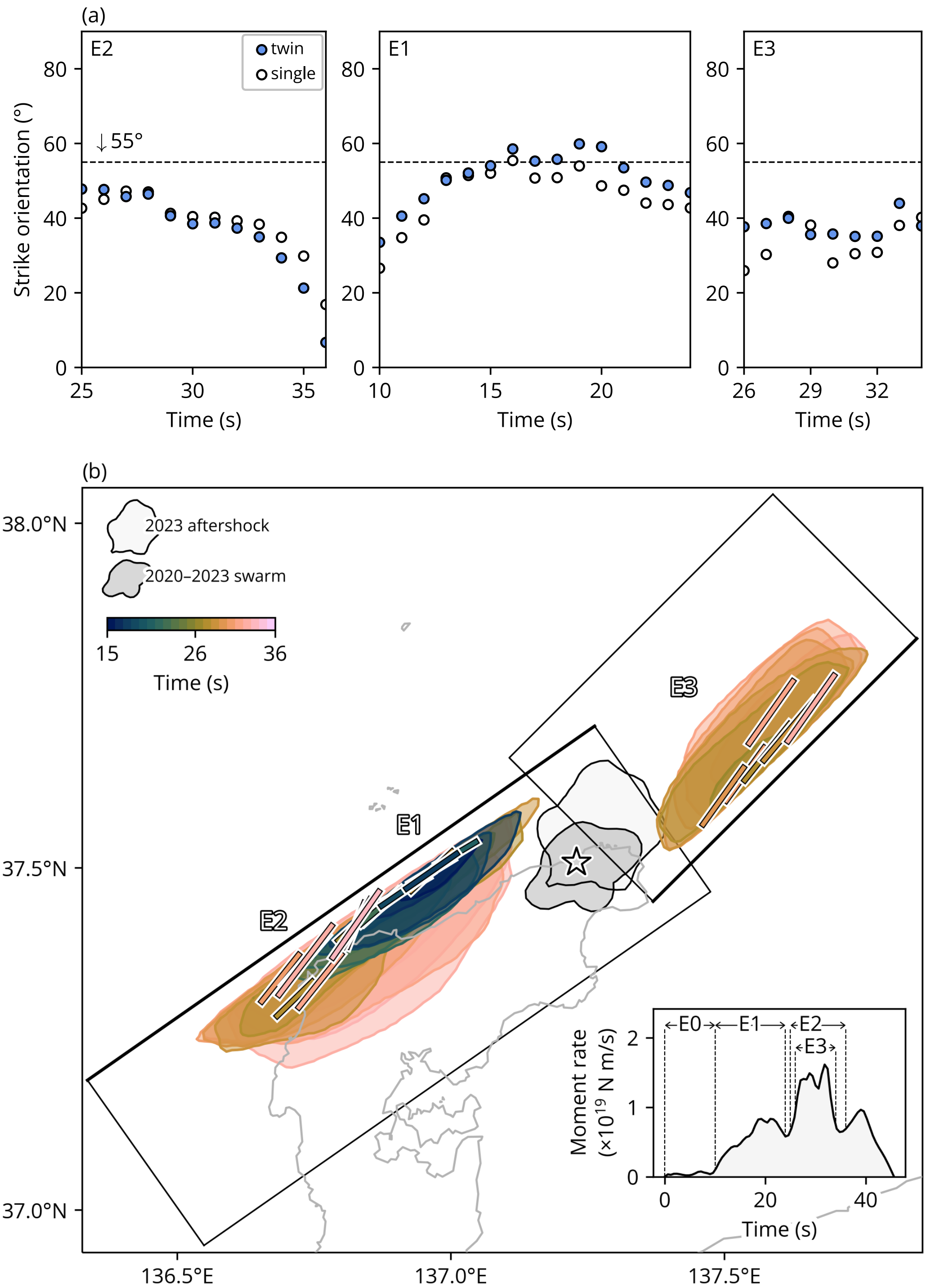


**Figure 4.** (a) The evolution of strike orientations for the twin and single fault models, focusing on the E1–E3 rupture episodes. (b) The summary of potency-rate density distributions and the corresponding strike orientations. The colored contours show the areas of > 50% of the maximum potency rate from 15 to 36 s in the western segment and from 26 to 33 s in the eastern segment. The bar represents the strike orientation for the maximum potency rate in the corresponding time window. The inset shows the moment rate function.

## References

Abercrombie, R., & Mori, J. (1994). Local observations of the onset of a large earthquake: 28 June 1992 Landers, California. *Bull. Seismol. Soc. Am.*, *84*(3), 725–734. doi:10.1785/BSSA0840030725

AIST. (2012). *Active Fault Database of Japan.* (https://gbank.gsj.jp/activefault/index_e_gmap.html)

Albuquerque Seismological Laboratory (ASL)/USGS. (1992). *New China Digital Seismograph Network.* International Federation of Digital Seismograph Networks. doi:10.7914/SN/IC

Albuquerque Seismological Laboratory/USGS. (2014). *Global Seismograph Network (GSN - IRIS/USGS).* International Federation of Digital Seismograph Networks. doi:10.7914/SN/IU

Amezawa, Y., Hiramatsu, Y., Miyakawa, A., Imanishi, K., & Otsubo, M. (2023). Long-Living Earthquake Swarm and Intermittent Seismicity in the Northeastern Tip of the Noto Peninsula, Japan. *Geophys. Res. Lett.*, *50*(8). doi:10.1029/2022GL102670

Aochi, H., & Madariaga, R. (2003). The 1999 Izmit, Turkey, Earthquake: Nonplanar Fault Structure, Dynamic Rupture Process, and Strong Ground Motion. *Bull. Seismol. Soc. Am.*, *93*(3), 1249-1266. doi:10.1785/0120020167

Bao, H., Ampuero, J.-P., Meng, L., Fielding, E. J., Liang, C., Milliner, C. W. D., . . . Huang, H. (2019). Early and persistent supershear rupture of the 2018 magnitude 7.5 Palu earthquake. *Nat. Geosci.*, *12*(3), 200–205. doi:10.1038/s41561-018-0297-z

Beyreuther, M., Barsch, R., Krischer, L., Megies, T., Behr, Y., & Wassermann, J. (2010). ObsPy: A Python Toolbox for Seismology. *Seismol. Res. Lett.*, *81*(3), 530–533. doi:10.1785/gssrl.81.3.530

Chu, S. X., Tsai, V. C., Trugman, D. T., & Hirth, G. (2021). Fault Interactions Enhance High-Frequency Earthquake Radiation. *Geophys. Res. Lett.*, *48*(20), 1–10. Retrieved from https://onlinelibrary.wiley.com/doi/10.1029/2021GL095271 doi:10.1029/2021GL095271

Crameri, F. (2018). Geodynamic diagnostics, scientific visualisation and StagLab 3.0. *Geosci. Model Dev.*, *11*(6), 2541–2562. doi:10.5194/gmd-11-2541-2018

Crameri, F., Shephard, G. E., & Heron, P. J. (2020). The misuse of colour in science communication. *Nat. Commun.*, *11*(1), 5444. doi:10.1038/s41467-020-19160-7

Ding, X., Xu, S., Xie, Y., Van den Ende, M., Premus, J., & Ampuero, J.-P. (2023). The sharp turn: Backward rupture branching during the 2023 Mw 7.8 Kahramanmaraş (Türkiye) earthquake. *Seismica*, *2*(3). doi:10.26443/seismica.v2i3.1083

Dublanchet, P., & De Barros, L. (2021). Dual Seismic Migration Velocities in Seismic Swarms. *Geophys. Res. Lett.*, *48*(1), 1–10. doi:10.1029/2020GL090025

Dutta, R., Jónsson, S., & Vasyura-Bathke, H. (2021). Simultaneous Bayesian Estimation of Non-Planar Fault Geometry and Spatially-Variable Slip. *J. Geophys. Res. Solid Earth*, *126*(7), 1–28. doi:10.1029/2020JB020441

Dziewonski, A. M., Chou, T.-A., & Woodhouse, J. H. (1981). Determination of earthquake source parameters from waveform data for studies of global and regional seismicity. *J. Geophys. Res. Solid Earth*, *86*(B4), 2825–2852.

doi:10.1029/JB086iB04p02825

Ekström, G., Nettles, M., & Dziewoński, A. (2012). The global CMT project 2004–2010: Centroid-moment tensors for 13,017 earthquakes. *Phys. Earth Planet. Inter.*, *200-201*, 1–9. doi:10.1016/j.pepi.2012.04.002

Ellsworth, W. L., & Beroza, G. C. (1995). Seismic Evidence for an Earthquake Nucleation Phase. *Science*, *268*(5212), 851–855. doi:10.1126/science.268.5212.851

Elson, P., de Andrade, E. S., Lucas, G., May, R., Hattersley, R., Campbell, E., ... Herzmann, D. (2022). *Scitools/cartopy: v0.21.1.* Zenodo. doi:10.5281/zenodo.7430317

Fan, W., Bassett, D., Jiang, J., Shearer, P. M., & Ji, C. (2017). Rupture evolution of the 2006 Java tsunami earthquake and the possible role of splay faults. *Tectonophysics*, *721*(28), 143–150. doi:10.1016/j.tecto.2017.10.003

Fan, W., Shearer, P. M., Ji, C., & Bassett, D. (2016). Multiple branching rupture of the 2009 Tonga-Samoa earthquake. *J. Geophys. Res. Solid Earth*, *121*(8), 5809–5827. doi:10.1002/2016JB012945

Fire and Disaster Management Agency. (2024). Damage Caused by the Noto Peninsula Earthquake of 2024 and the Response of Fire-Fighting Agencies. (Report No. 81). (https://www.fdma.go.jp/disaster/info/2024/)

Fujii, Y., & Satake, K. (2024). Slip distribution of the 2024 Noto Peninsula earthquake (MJMA 7.6) estimated from tsunami waveforms and GNSS data. *Earth, Planets Sp.*, *76*(1), 44. doi:10.1186/s40623-024-01991-z

Fukuda, J. (2018). Variability of the Space-Time Evolution of Slow Slip Events Off the Boso Peninsula, Central Japan, From 1996 to 2014. *J. Geophys. Res. Solid Earth*, *123*(1), 732–760. doi:10.1002/2017JB014709

Gasperini, P., & Vannucci, G. (2003). FPSPACK: a package of FORTRAN subroutines to manage earthquake focal mechanism data. *Comput. Geosci.*, *29*(7), 893–901. doi:10.1016/S0098-3004(03)00096-7

GEOFON Data Centre. (1993). *GEOFON Seismic Network.* Deutsches GeoForschungsZentrum GFZ. doi:10.14470/TR560404

Geospatial Information Authority of Japan. (2024). *Crustal deformation associated with the 2024 Noto Peninsula Earthquake Based on Analysis of ALOS-2.* (https://www.gsi.go.jp/uchusokuchi/20240101noto_insar.html)

Hamling, I. J., Hreinsdóttir, S., Clark, K., Elliott, J., Liang, C., Fielding, E., ... Stirling, M. (2017). Complex multifault rupture during the 2016 Mw 7.8 Kaikōura earthquake, New Zealand. *Science*, *356*(6334). doi:10.1126/science.aam7194

Heimann, S., Kriegerowski, M., Isken, M., Cesca, S., Daout, S., Grigoli, F., ... Vasyura-Bathke, H. (2017). *Pyrocko - An open-source seismology toolbox and library.* GFZ Data Services. doi:10.5880/GFZ.2.1.2017.001

Hicks, S. P., Okuwaki, R., Steinberg, A., Rychert, C. A., Harmon, N., Abercrombie, R. E., ... Sudhaus, H. (2020). Back-propagating supershear rupture in the 2016 Mw 7.1 Romanche transform fault earthquake. *Nat. Geosci.*, *13*(9), 647–653. doi:10.1038/s41561-020-0619-9

Hicks, S. P., & Rietbrock, A. (2015). Seismic slip on an upper-plate normal fault during a large subduction megathrust rupture. *Nat. Geosci.*, *8*(12), 955–960. doi:10.1038/ngeo2585

Hiramatsu, Y., Moriya, K., Kamiya, T., Kato, M., & Nishimura, T. (2008). Fault model of the 2007 Noto Hanto earthquake estimated from coseismic deformation obtained by the distribution of littoral organisms and GPS: Implication for neotectonics in the northwestern Noto Peninsula. *Earth, Planets Sp.*, *60*(9), 903–913. doi:10.1186/BF03352846

Hunter, J. D. (2007). Matplotlib: A 2D Graphics Environment. *Comput. Sci. Eng.*, *9*(3), 90–95. doi:10.1109/MCSE.2007.55

Im, K., & Avouac, J.-P. (2023). Cascading foreshocks, aftershocks and earthquake swarms in a discrete fault network. *Geophys. J. Int.*, *235*(1), 831–852. doi:10.1093/gji/ggad278

Institut De Physique Du Globe De Paris (IPGP), & Ecole Et Observatoire Des Sciences De La Terre De Strasbourg (EOST). (1982). *GEOSCOPE, French Global Network of broad band seismic stations.* Institut de physique du globe de Paris (IPGP), Université de Paris. doi:10.18715/GEOSCOPE.G

Japan Meteorological Agency. (2024). *The Seismological Bulletin of Japan.* (https://www.data.jma.go.jp/svd/eqev/data/bulletin/hypo_e.html)

Kato, A. (2024). Implications of Fault-Valve Behavior From Immediate Aftershocks Following the 2023 M j 6.5 Earthquake Beneath the Noto Peninsula, Central Japan . *Geophys. Res. Lett.*, *51*(1), 1–10. doi:10.1029/2023gl106444

Kato, A., & Nakagawa, S. (2014). Multiple slow-slip events during a foreshock sequence of the 2014 Iquique, Chile M w 8.1 earthquake. *Geophys. Res. Lett.*, *41*(15), 5420–5427. doi:10.1002/2014GL061138

Kennett, B. L., Engdahl, E. R., & Buland, R. (1995). Constraints on seismic velocities in the Earth from traveltimes. *Geophys. J. Int.*, *122*(1), 108–124. doi:10.1111/j.1365-246X.1995.tb03540.x

Kikuchi, M., & Kanamori, H. (1991). Inversion of complex body waves-III. *Bull. Seism. Soc. Am.*, *81*(6), 2335–2350. doi:10.1785/BSSA0810062335

Kuge, K., Zhang, J., & Kikuchi, M. (1996). The 12 July 1993 Hokkaido-Nansei-Oki, Japan, earthquake: Effects of source complexity on surface-wave radiation. *Bull. Seismol. Soc. Am.*, *86*(2), 505–518. doi:10.1785/BSSA0860020505

Kutschera, F., Jia, Z., Oryan, B., Wing Ching Wong, J., Fan, W., & Gabriel, A.-A. (2024). Rapid earthquake-tsunami modeling: The multi-event, multi-segment complexity of the 2024 Mw 7.5 Noto Peninsula Earthquake governs tsunami generation. *EarthArXiv*. doi:10.31223/X5ZX1S

Laske, G., Masters, T. G., Ma, Z., & Pasyanos, M. (2013). Update on CRUST1.0 - A 1-degree Global Model of Earth's Crust. *Geophys. Res. Abstr. 15, Abstr. EGU2013-2658*, *15*, Abstract EGU2013–2658. (https://igppweb.ucsd.edu/~gabi/crust1.html)

Lay, T., Ye, L., Bai, Y., Cheung, K. F., & Kanamori, H. (2018). The 2018 MW 7.9 Gulf of Alaska Earthquake: Multiple Fault Rupture in the Pacific Plate. *Geophys. Res. Lett.*, *45*(18), 9542–9551. doi:10.1029/2018GL079813

MedNet Project Partner Institutions. (1990). *Mediterranean Very Broadband Seismographic Network (MedNet).* Istituto Nazionale di Geofisica e Vulcanologia (INGV). doi:10.13127/SD/FBBBTDTD6Q

Meng, L., Ampuero, J. P., Stock, J., Duputel, Z., Luo, Y., & Tsai, V. C. (2012). Earthquake in a maze: Compressional rupture branching during the

2012 Mw 8.6 Sumatra earthquake. *Science*, *337*(6095), 724–726. doi:10.1126/science.1224030

Met Office. (2015). *Cartopy: a cartographic python library with a Matplotlib interface.* doi:10.5281/zenodo.1182735

Ministry of Land, Infrastructure, Transport and Tourism, Japan. (2014). A report by working group on large earthquakes in the Sea of Japan. (https://www.mlit.go.jp/river/shinngikai_blog/daikibojishinchousa/)

Mizutani, A., Adriano, B., Mas, E., & Koshimura, S. (2024). Fault Model of the 2024 Noto Peninsula Earthquake Based on Aftershock, Tsunami, and GNSS Data. *Res. Sq.*. doi:10.21203/rs.3.rs-4167995/v1

NASA JPL. (2013). NASA Shuttle Radar Topography Mission Global 1 arc second [Data set]. *NASA EOSDIS Land Processes Distributed Active Archive Center*. doi:10.5067/MEaSUREs/SRTM/SRTMGL1.003

National Research Institute for Earth Science and Disaster Resilience. (2019a). *NIED F-net.* doi:10.17598/NIED.0005

National Research Institute for Earth Science and Disaster Resilience. (2019b). *NIED K-NET, KiK-net.* doi:10.17598/NIED.0004

National Research Institute for Earth Science and Disaster Resilience. (2024). *NIED Earthquake Mechanism Search.* (https://www.fnet.bosai.go.jp/event/search.php?LANG=en)

Nishikawa, T., Nishimura, T., & Okada, Y. (2021). Earthquake Swarm Detection Along the Hikurangi Trench, New Zealand: Insights Into the Relationship Between Seismicity and Slow Slip Events. *J. Geophys. Res. Solid Earth*, *126*(4), 1–31. doi:10.1029/2020JB020618

Nishimura, T., Hiramatsu, Y., & Ohta, Y. (2023). Episodic transient deformation revealed by the analysis of multiple GNSS networks in the Noto Peninsula, central Japan. *Sci. Rep.*, *13*(1), 1–11. doi:10.1038/s41598-023-35459-z

Nissen, E., Elliott, J. R., Sloan, R. A., Craig, T. J., Funning, G. J., Hutko, A., … Wright, T. J. (2016). Limitations of rupture forecasting exposed by instantaneously triggered earthquake doublet. *Nat. Geosci.*, *9*(4), 330–336. doi:10.1038/ngeo2653

Northern California Earthquake Data Center. (2014). *Berkeley Digital Seismic Network (BDSN).* Northern California Earthquake Data Center. doi:10.7932/BDSN

Ohara, K., Yagi, Y., & Okuwaki, R. (2024). Complex rupture evolution of the 2007 Martinique earthquake: a non-double-couple event in the Caribbean Sea. *Geophys. J. Int.*, *236*(3), 1743–1752. doi:10.1093/gji/ggae024

Ohara, K., Yagi, Y., Yamashita, S., Okuwaki, R., Hirano, S., & Fukahata, Y. (2023). Complex evolution of the 2016 Kaikoura earthquake revealed by teleseismic body waves. *Prog. Earth Planet. Sci.*, *10*(1), 35. doi:10.1186/s40645-023-00565-z

Okamura, Y., Watanabe, M., Morijiri, R., & Satoh, M. (1995). Rifting and basin inversion in the eastern margin of the Japan Sea. *Isl. Arc*, *4*(3), 166–181. doi:10.1111/j.1440-1738.1995.tb00141.x

Okuwaki, R., & Fan, W. (2022). Oblique Convergence Causes Both Thrust and Strike-Slip Ruptures During the 2021 M 7.2 Haiti Earthquake. *Geophys. Res.*

*Lett.*, *49*(2), 1–12. doi:10.1029/2021GL096373

Okuwaki, R., Yagi, Y., Aránguiz, R., González, J., & González, G. (2016). Rupture Process During the 2015 Illapel, Chile Earthquake: Zigzag-Along-Dip Rupture Episodes. *Pure Appl. Geophys.*, *173*(4), 1011–1020. doi:10.1007/s00024-016-1271-6

Okuwaki, R., Yagi, Y., Taymaz, T., & Hicks, S. P. (2023). Multi-Scale Rupture Growth With Alternating Directions in a Complex Fault Network During the 2023 South-Eastern Türkiye and Syria Earthquake Doublet. *Geophys. Res. Lett.*, *50*(12), 1–14. doi:10.1029/2023gl103480

Ragon, T., Sladen, A., & Simons, M. (2018). Accounting for uncertain fault geometry in earthquake source inversions – I: theory and simplified application. *Geophys. J. Int.*, *214*(2), 1174–1190. doi:10.1093/gji/ggy187

Ross, Z. E., Cochran, E. S., Trugman, D. T., & Smith, J. D. (2020). 3D fault architecture controls the dynamism of earthquake swarms. *Science*, *368*(6497), 1357–1361. Retrieved from https://www.science.org/doi/10.1126/science.abb0779 doi:10.1126/science.abb0779

Ruiz, S., Metois, M., Fuenzalida, A., Ruiz, J., Leyton, F., Grandin, R., … Campos, J. (2014). Intense foreshocks and a slow slip event preceded the 2014 Iquique M w 8.1 earthquake. *Science*, *345*(6201), 1165–1169. doi:10.1126/science.1256074

Sato, H. (1994). The relationship between Late Cenozoic tectonic events and stress field and basin development in northeast Japan. *J. Geophys. Res. Solid Earth*, *99*(B11), 22261–22274. doi:10.1029/94JB00854

Satriano, C., Kiraly, E., Bernard, P., & Vilotte, J.-P. (2012). The 2012 Mw 8.6 Sumatra earthquake: Evidence of westward sequential seismic ruptures associated to the reactivation of a N-S ocean fabric. *Geophys. Res. Lett.*, *39*(15). doi:10.1029/2012GL052387

Shelly, D. R. (2024). Examining the Connections Between Earthquake Swarms, Crustal Fluids, and Large Earthquakes in the Context of the 2020–2024 Noto Peninsula, Japan, Earthquake Sequence. *Geophys. Res. Lett.*, *51*(4). doi:10.1029/2023GL107897

Shelly, D. R., Ellsworth, W. L., & Hill, D. P. (2016). Fluid-faulting evolution in high definition: Connecting fault structure and frequency-magnitude variations during the 2014 Long Valley Caldera, California, earthquake swarm. *J. Geophys. Res. Solid Earth*, *121*(3), 1776–1795. doi:10.1002/2015JB012719

Shimizu, K., Yagi, Y., Okuwaki, R., & Fukahata, Y. (2020). Development of an inversion method to extract information on fault geometry from teleseismic data. *Geophys. J. Int.*, *220*(2), 1055–1065. doi:10.1093/gji/ggz496

Shimizu, K., Yagi, Y., Okuwaki, R., & Fukahata, Y. (2021). Construction of fault geometry by finite-fault inversion of teleseismic data. *Geophys. J. Int.*, *224*(2), 1003–1014. doi:10.1093/gji/ggaa501

Tadapansawut, T., Okuwaki, R., Yagi, Y., & Yamashita, S. (2021). Rupture Process of the 2020 Caribbean Earthquake Along the Oriente Transform Fault, Involving Supershear Rupture and Geometric Complexity of Fault. *Geophys. Res. Lett.*, *48*(1), 1–9. doi:10.1029/2020GL090899

Taufiqurrahman, T., Gabriel, A. A., Li, D., Ulrich, T., Li, B., Carena, S., ... Gallovič, F. (2023). Dynamics, interactions and delays of the 2019 Ridgecrest rupture sequence. *Nature*, *618*(7964), 308–315. doi:10.1038/s41586-023-05985-x

University of Tokyo, Earthquake Research Institute (Todai, ERI), Japan. (1989). *Pacific21 (ERI/STA).* International Federation of Digital Seismograph Networks. (https://www.fdsn.org/networks/detail/PS/)

Vallée, M., Xie, Y., Grandin, R., Villegas-Lanza, J. C., Nocquet, J. M., Vaca, S., ... Rolandone, F. (2023). Self-reactivated rupture during the 2019 Mw = 8 northern Peru intraslab earthquake. *Earth Planet. Sci. Lett.*, *601*, 117886. doi:10.1016/j.epsl.2022.117886

Vasyura-Bathke, H., Steinberg, A., Krüger, F., Feng, G., Mai, P. M., & Jónsson, S. (2024). Discontinuous transtensional rupture during the Mw 7.2 1995 Gulf of Aqaba earthquake. *Seismica*, *3*(1). doi:10.26443/seismica.v3i1.1135

Vidale, J. E., & Shearer, P. M. (2006). A survey of 71 earthquake bursts across southern California: Exploring the role of pore fluid pressure fluctuations and aseismic slip as drivers. *J. Geophys. Res. Solid Earth*, *111*(B5), 1–12. doi:10.1029/2005JB004034

Wang, B., & Barbot, S. (2023). Pulse-like ruptures, seismic swarms, and tremorgenic slow-slip events with thermally activated friction. *Earth Planet. Sci. Lett.*, *603*, 117983. doi:10.1016/j.epsl.2022.117983

Wessel, P., Luis, J. F., Uieda, L., Scharroo, R., Wobbe, F., Smith, W. H. F., & Tian, D. (2019). The Generic Mapping Tools Version 6. *Geochemistry, Geophys. Geosystems*, *20*(11), 5556–5564. doi:10.1029/2019GC008515

Yagi, Y., & Fukahata, Y. (2011). Introduction of uncertainty of Green's function into waveform inversion for seismic source processes. *Geophys. J. Int.*, *186*(2), 711–720. doi:10.1111/j.1365-246X.2011.05043.x

Yagi, Y., Okuwaki, R., Enescu, B., Hirano, S., Yamagami, Y., Endo, S., & Komoro, T. (2014). Rupture process of the 2014 Iquique Chile Earthquake in relation with the foreshock activity. *Geophys. Res. Lett.*, *41*(12), 4201–4206. doi:10.1002/2014GL060274

Yagi, Y., Okuwaki, R., Enescu, B., & Lu, J. (2023). Irregular rupture process of the 2022 Taitung, Taiwan, earthquake sequence. *Sci. Rep.*, *13*(1), 1107. doi:10.1038/s41598-023-27384-y

Yagi, Y., Okuwaki, R., Hirano, S., Enescu, B., Chikamori, M., & Yamaguchi, R. (2024). Barrier-Induced Rupture Front Disturbances during the 2023 Morocco Earthquake. *Seismol. Res. Lett.*, 1–8. doi:10.1785/0220230357

Yamashita, S., Yagi, Y., & Okuwaki, R. (2022). Irregular rupture propagation and geometric fault complexities during the 2010 Mw 7.2 El Mayor-Cucapah earthquake. *Sci. Rep.*, *12*(1), 4575. doi:10.1038/s41598-022-08671-6

Yamashita, S., Yagi, Y., Okuwaki, R., Shimizu, K., Agata, R., & Fukahata, Y. (2022). Potency density tensor inversion of complex body waveforms with time-adaptive smoothing constraint. *Geophys. J. Int.*, *231*(1), 91–107. doi:10.1093/gji/ggac181

Yoshida, K., Uchida, N., Matsumoto, Y., Orimo, M., Okada, T., Hirahara, S., ... Hino, R. (2023). Updip Fluid Flow in the Crust of the Northeastern Noto Peninsula, Japan, Triggered the 2023 Mw 6.2 Suzu Earthquake During Swarm Activity.

*Geophys. Res. Lett.*, *50*(21). doi:10.1029/2023GL106023

Yoshida, K., Uno, M., Matsuzawa, T., Yukutake, Y., Mukuhira, Y., Sato, H., & Yoshida, T. (2023). Upward Earthquake Swarm Migration in the Northeastern Noto Peninsula, Japan, Initiated From a Deep Ring-Shaped Cluster: Possibility of Fluid Leakage From a Hidden Magma System. *J. Geophys. Res. Solid Earth*, *128*(6), 1–22. doi:10.1029/2022JB026047

Zhu, W., Allison, K. L., Dunham, E. M., & Yang, Y. (2020). Fault valving and pore pressure evolution in simulations of earthquake sequences and aseismic slip. *Nat. Commun.*, *11*(1), 4833. doi:10.1038/s41467-020-18598-z

Supporting Information for

# A Multiplex Rupture Sequence under Complex Fault Network due to Preceding Earthquake Swarms during the 2024 Mw 7.5 Noto Peninsula, Japan, Earthquake

**Ryo Okuwaki[1], Yuji Yagi[1], Asuka Murakami[2], Yukitoshi Fukahata[3]**

[1]Institute of Life and Environmental Sciences, University of Tsukuba, Tsukuba, Ibaraki 305-8572, Japan
[2]Graduate School of Science and Technology, University of Tsukuba, Tsukuba, Ibaraki 305-8572, Japan
[3]Disaster Prevention Research Institute, Kyoto University, Uji, Kyoto, 611-0011, Japan

**Contents**



Corresponding author: Ryo Okuwaki, `rokuwaki@geol.tsukuba.ac.jp`

**Table S1.** Near-source structure used for calculating Green's functions, adopted from ak135 model (Kennett et al., 1995).

| $V_P$ (km/s) | $V_S$ (km/s) | Density (g/cm$^3$) | Thickness (km) |
|---|---|---|---|
| 5.80 | 3.46 | 2.45 | 20.0 |
| 6.50 | 3.85 | 2.71 | 15.0 |
| 8.04 | 4.48 | 3.30 | - (below moho) |

**Table S2.** Near-source structure used for calculating Green's functions, adopted from CRUST1.0 model (Laske et al., 2013).

| $V_P$ (km/s) | $V_S$ (km/s) | Density (g/cm$^3$) | Thickness (km) |
|---|---|---|---|
| 6.00 | 3.50 | 2.72 | 6.22 |
| 6.60 | 3.80 | 2.86 | 7.92 |
| 7.10 | 3.90 | 3.05 | 13.20 |
| 7.70 | 4.29 | 3.17 | - (below moho) |

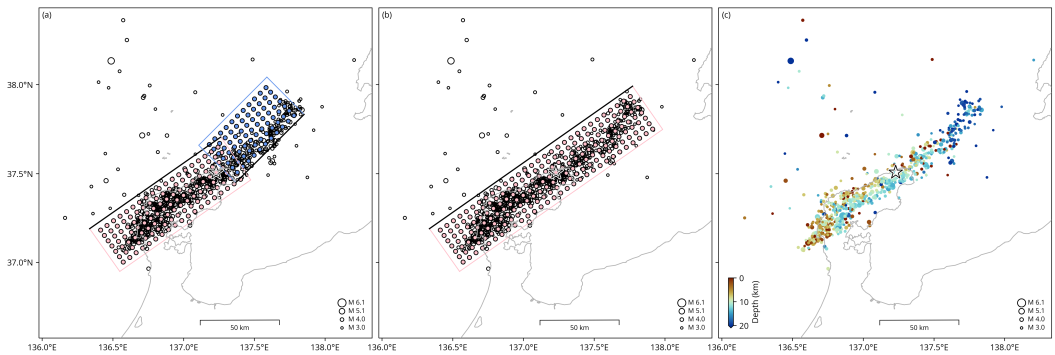


**Figure S1.** Model geometries for the (a) twin and (b) single fault models. The blue and pink dots are the locations of source elements. The star shows the initial rupture point. The black circles show the 24-hour aftershocks (Japan Meteorological Agency, 2024). (c) The 24-hour aftershocks (Japan Meteorological Agency, 2024) colored by depth.

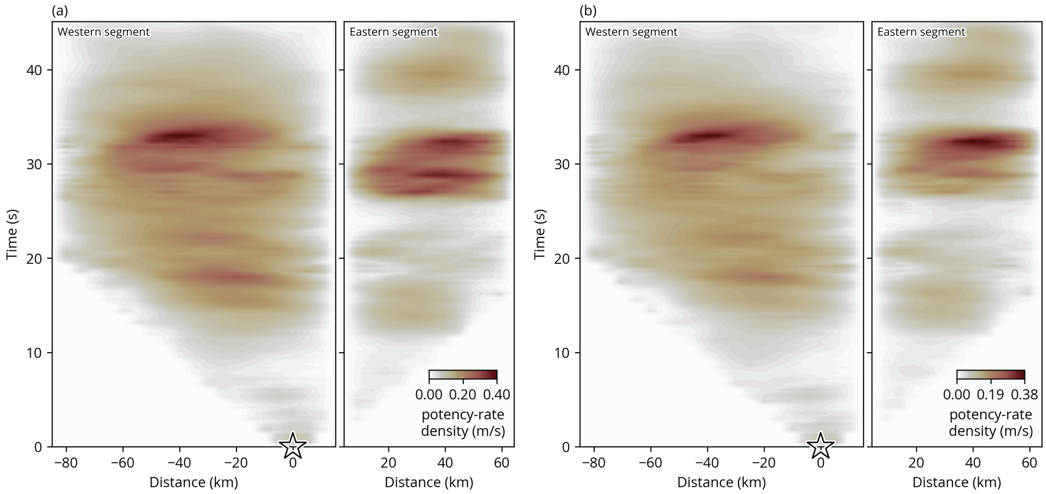


**Figure S2.** Comparison of solutions using the (a) ak135 and (b) CRUST1.0 models (Tables S1 and S2). The figure style is the same as Fig. 2.

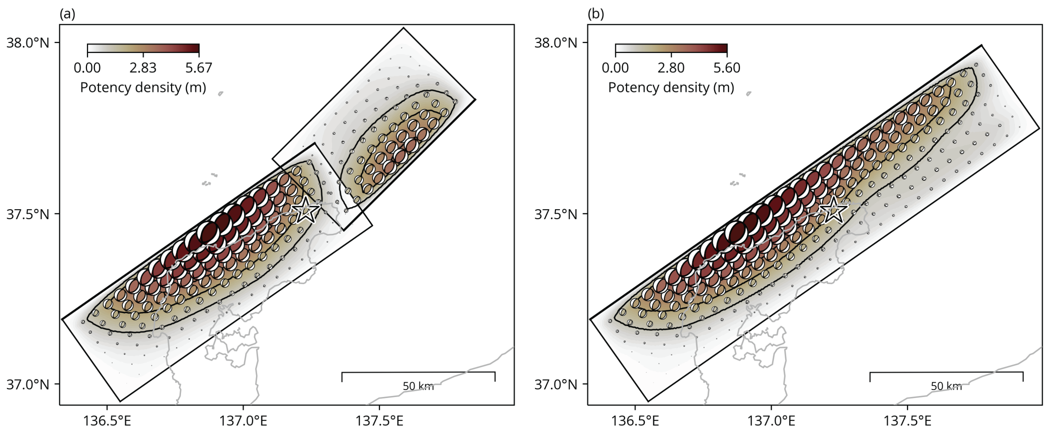


**Figure S3.** Comparison of potency density tensor distributions for the (a) twin and (b) single fault models. The figure style is the same as Fig. 2. The black contour outlines potency every 1.1 m for both the models.

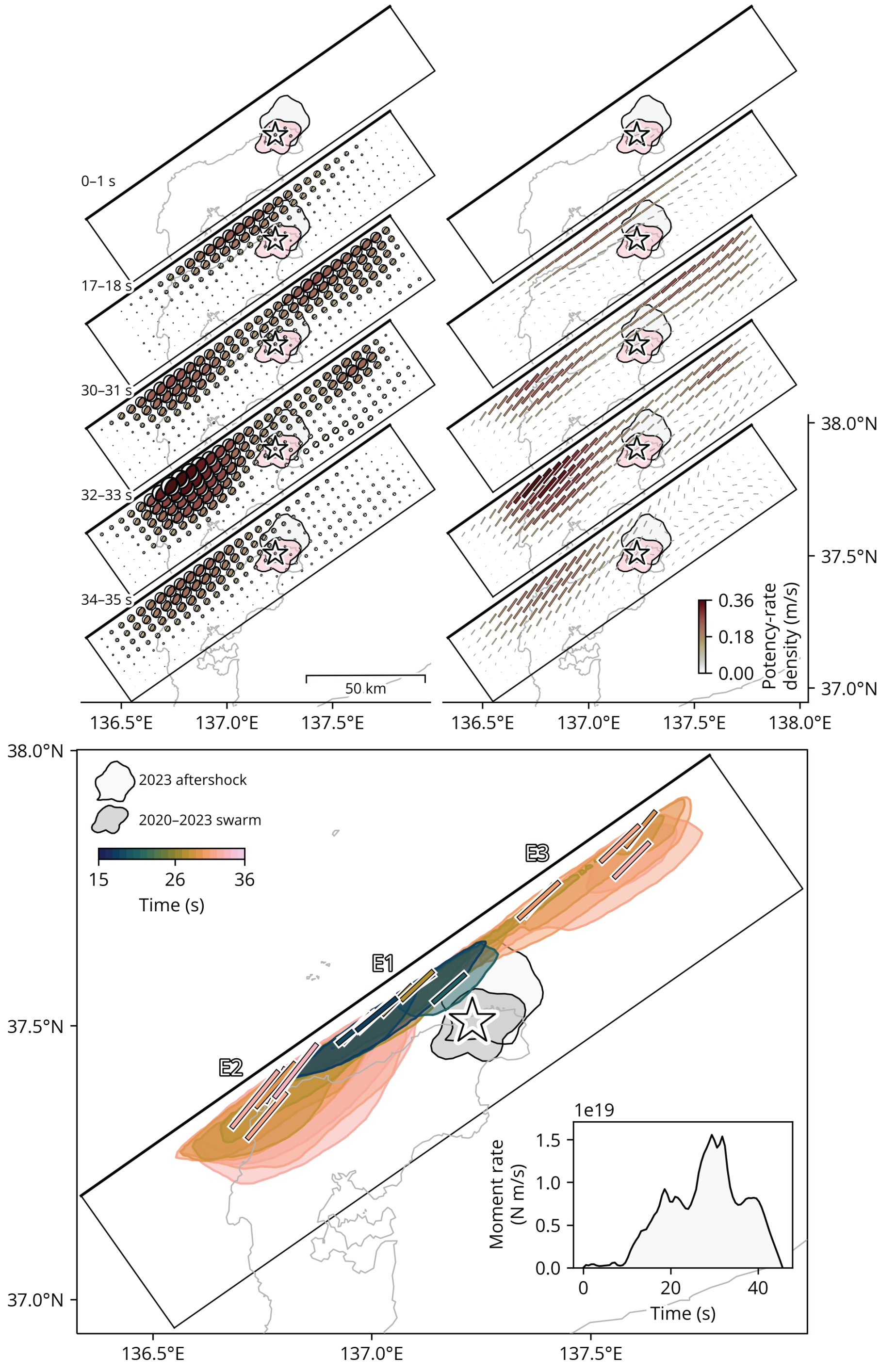


**Figure S4.** The upper panels show the selected snapshots of the potency-rate density tensors and the corresponding strike orientation distributions. The bar represents the strike orientation, which is one of the two possible nodal planes of the best-fitting double couple solution that minimizes the inner product of fault-normal vectors of the candidate plane and the corresponding model plane. The lower panel shows the summary of the selected snapshots of the potency-rate density distribution and the strike orientations. The figure style and legends are the same as Fig. 4. The full snapshots can be seen in Movie S2.

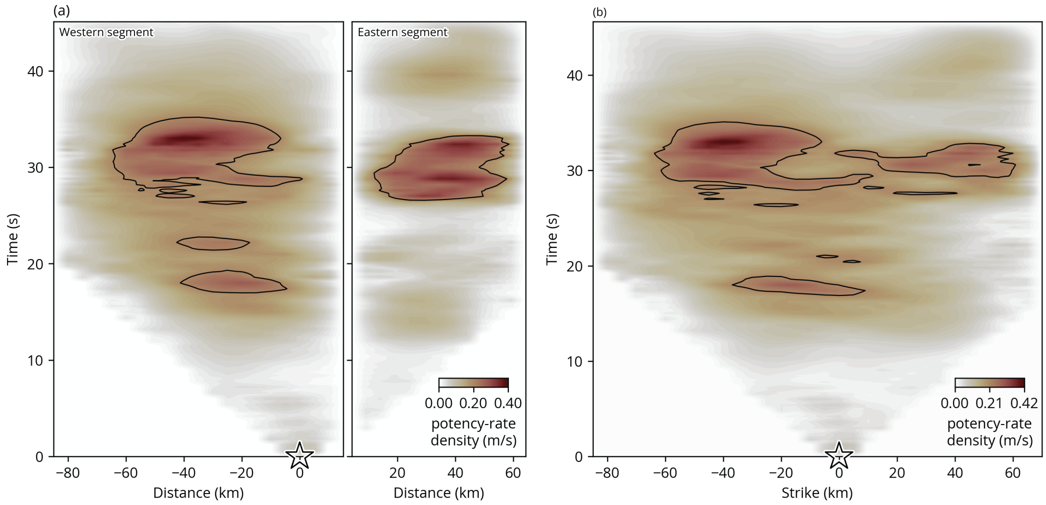


**Figure S5.** Comparison of solutions built upon the (a) twin and (b) single model faults. The black contours highlight the loci of > 50% of maximum potency rate. The figure style is the same as Fig. 2.

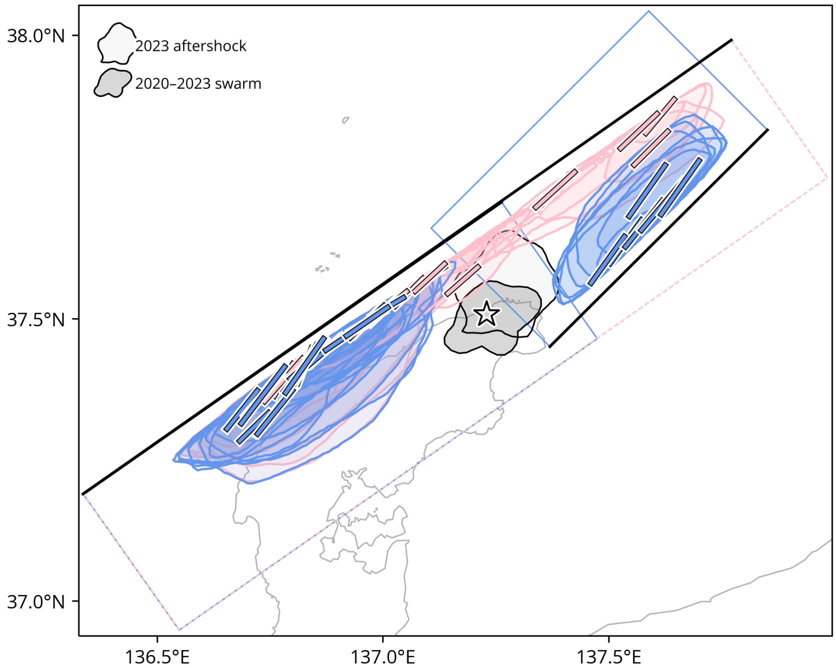


**Figure S6.** Comparison of spatiotemporal distributions of potency rate density and the corresponding strike orientation from the twin (blue) and single (pink) fault models. The figure style and legends are the same as Figs. 4 and S4.

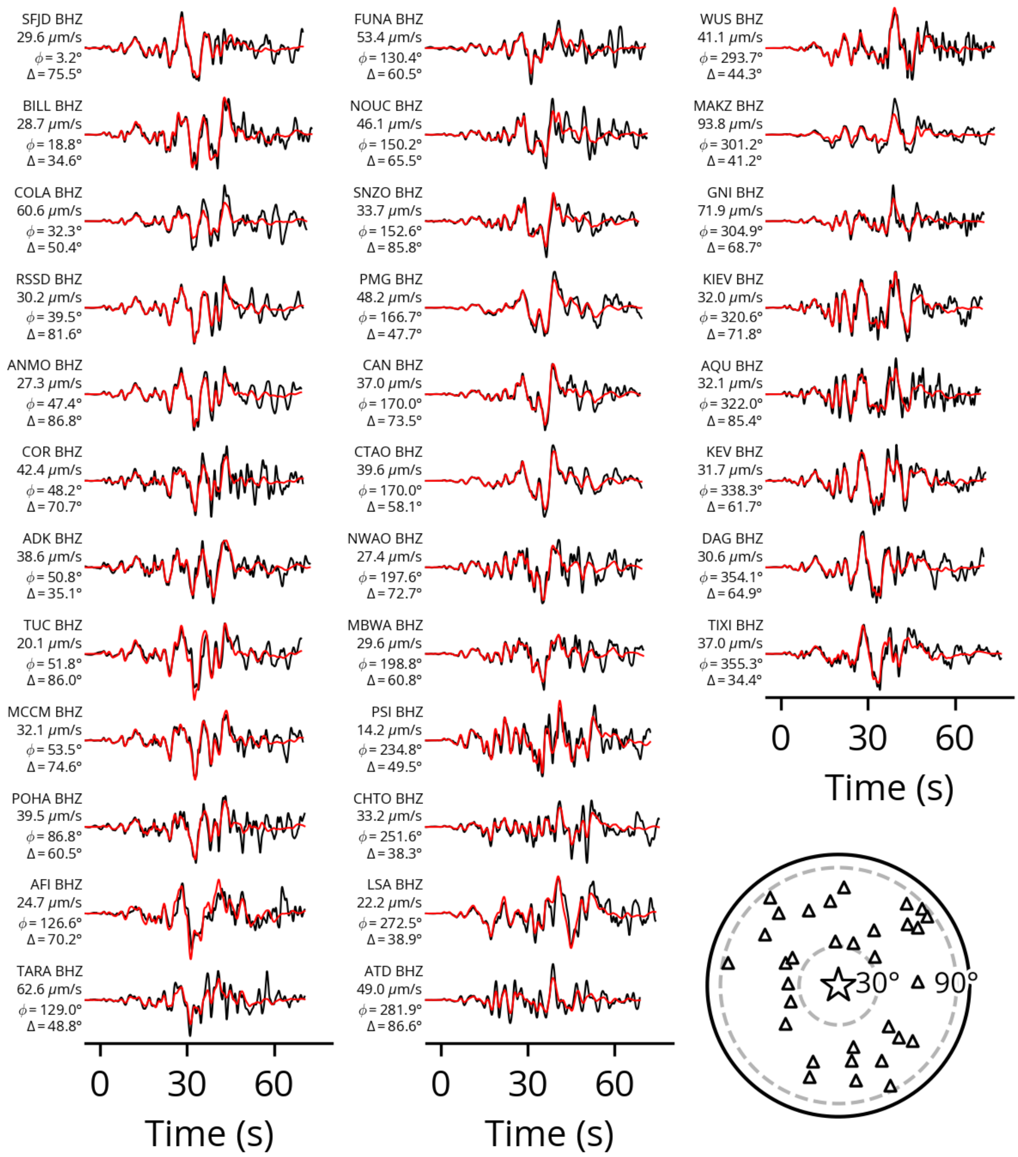


**Figure S7.** Waveform fits of the twin fault model. The black and red traces are the observed and synthetic waveforms. The station code and channel, the maximum amplitude of observed waveform, the station azimuth ($\phi$), and the epicentral distance ($\Delta$) are shown on the left of each panel. The bottom map is an azimuthal equidistant projection of the station distribution (triangle). The star shows the epicenter. The dashed lines are the epicentral distances at 30° and 90°.

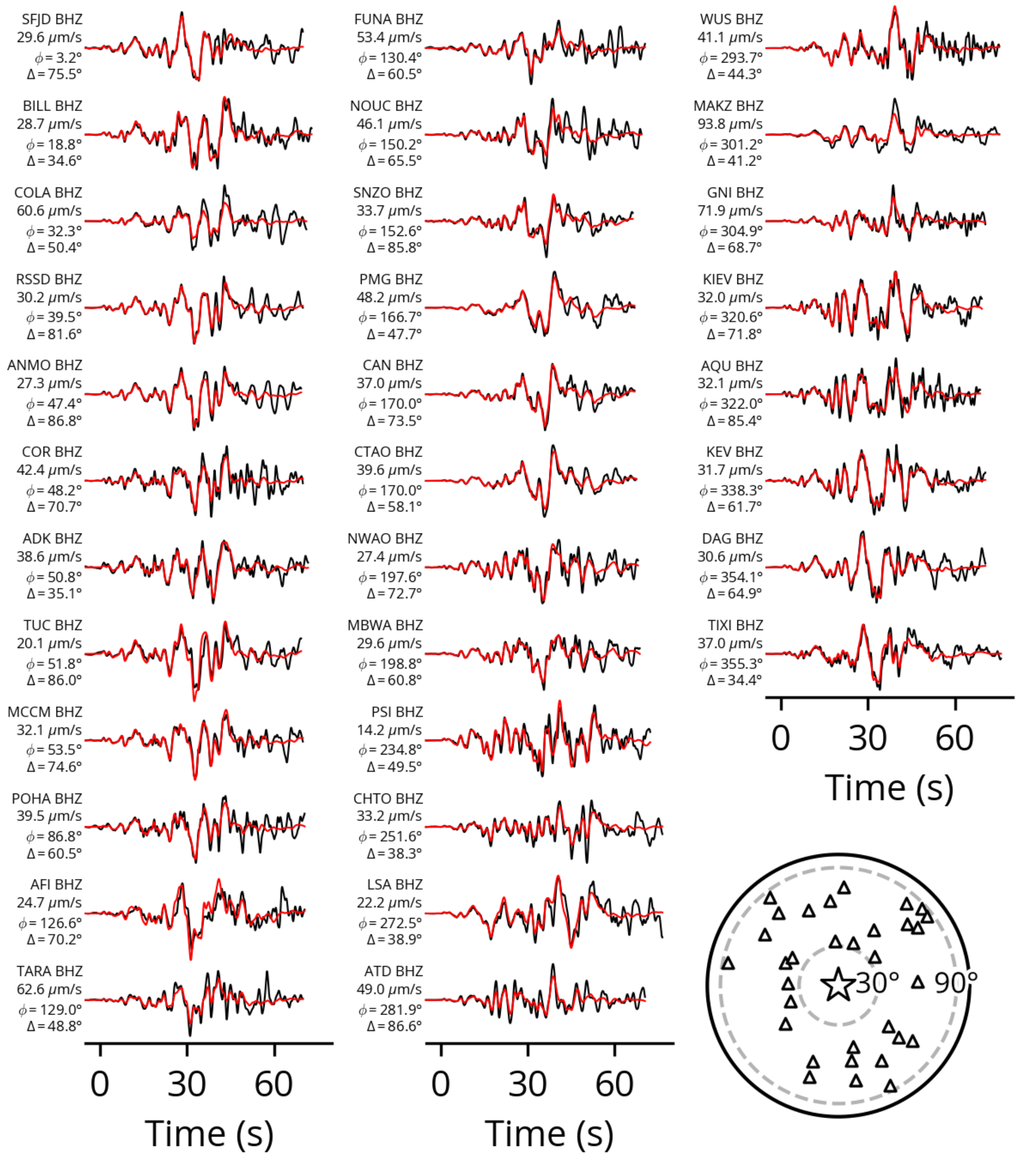


**Figure S8.** Waveform fits of the single fault model. The black and red traces are the observed and synthetic waveforms. The station code and channel, the maximum amplitude of observed waveform, the station azimuth ($\phi$), and the epicentral distance ($\Delta$) are shown on the left of each panel. The bottom map is an azimuthal equidistant projection of the station distribution (triangle). The star shows the epicenter. The dashed lines are the epicentral distances at 30° and 90°.

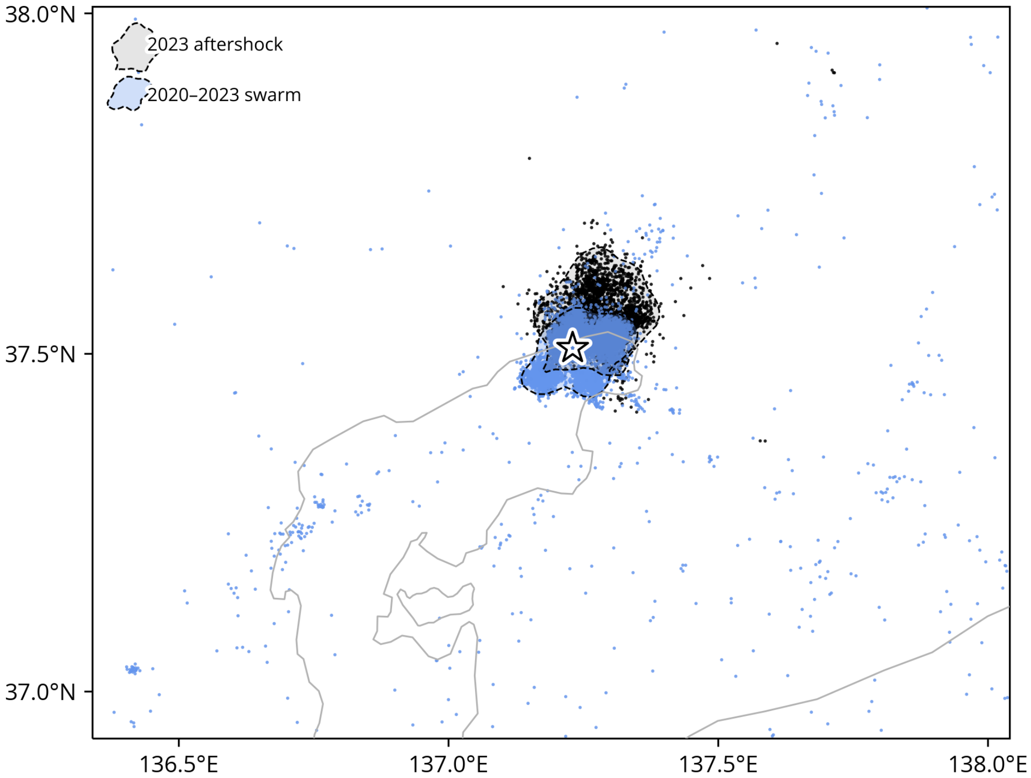


**Figure S9.** Summary of the 2020–2023 earthquake swarms (from 2020-11-01T00:00:00 to 2023-05-05T05:42:04 (UTC)) and the 2023 $M$ 6.5 aftershocks (from 2023-05-05T05:42:04 to 2023-05-12T05:42:04 (UTC)) (Japan Meteorological Agency, 2024) with $M_{\mathrm{JMA}} > 1$. The dots show the epicenters. The contours show the regions of the 2020–2023 earthquake swarms (blue) and the 1-week aftershock of the 2023 $M$ 6.5 earthquake (gray) based on the Gaussian kernel-density estimates, delimiting the areas with > 5% of the normalized density. The star shows the initial rupture point adopted for the source process modeling for the 2024 Noto Peninsula earthquake in this study.

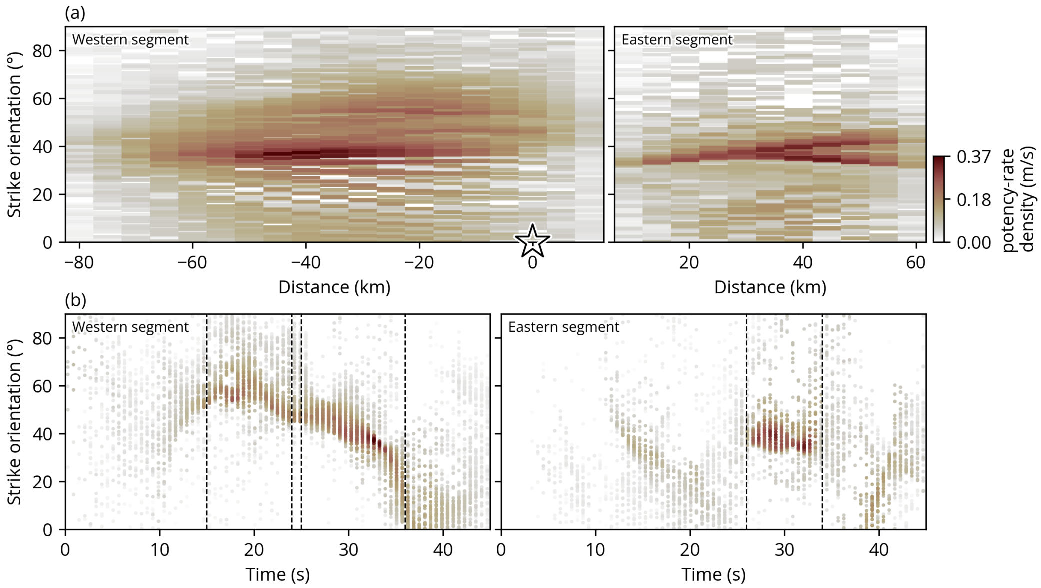


**Figure S10.** Spatiotemporal distribution of the strike orientations. (a) The abscissa is a distance from the initial rupture point along each model strike, and the ordinate is a strike orientation (a remainder of dividing the strike angle by 180°). The strike orientation is extracted from the resultant potency density tensor, selected from the one of the two possible nodal planes of the best-fitting double couple solution that minimizes the inner product of fault-normal vectors of the candidate plane and the corresponding model plane. The star represents the initial rupture point. (b) The abscissa is a time from the origin time, and the ordinate is a strike orientation. The dashed rectangles highlight the notable rupture domains that are displayed in Figs. 3 and 4.

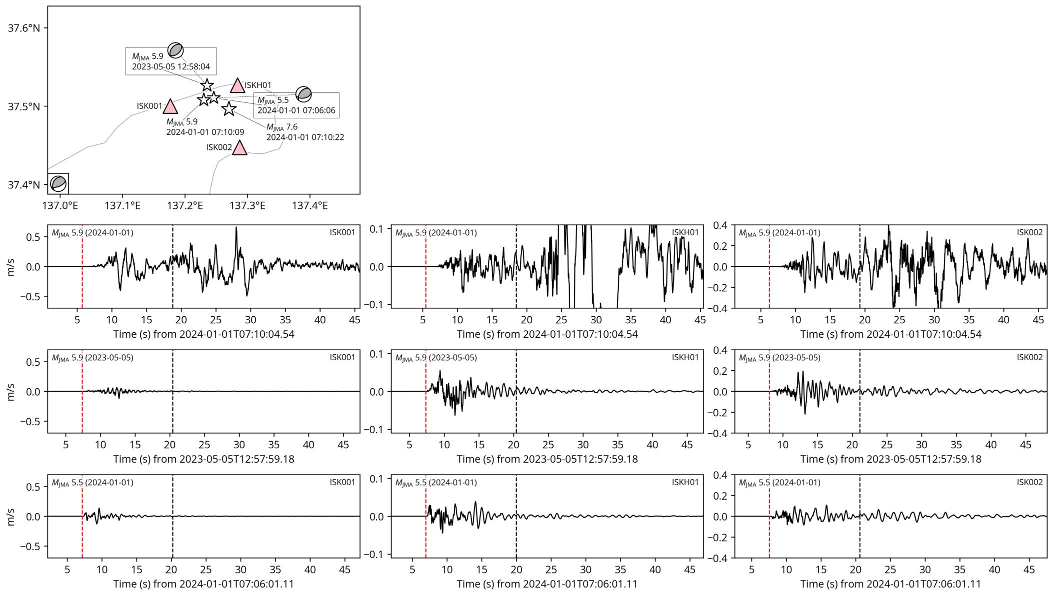


**Figure S11.** Compilation of the near-field records from the NIED K-NET and KiK-net (National Research Institute for Earth Science and Disaster Resilience, 2019b). The map shows the stations (triangles) and the JMA epicenters (stars) (Japan Meteorological Agency, 2024). The beachballs on a map show the lower-hemisphere projection of the moment tensors from the available NIED F-net moment tensor catalog (National Research Institute for Earth Science and Disaster Resilience, 2019a, 2024). The inset beachball shows the lower-hemisphere projection of the moment tensor obtained from the potency-rate density tensor for the maximum potency-rate density during the E0 episode (Fig. 2). The lower panels show the highpass (0.05 Hz) filtered vertical component of velocity records for the 2024 Noto Peninsula earthquake (second row) and other two earthquakes with similar sizes (third and fourth row). The red dashed line denotes the first phase arrival of the corresponding event. The black dashed line marks the relative origin time (13.03 s) between the $M_{\text{JMA}}$ 5.9 (2024-01-01) and 7.6 events.

**Movie S1.** Snapshots of the potency-rate density tensor distribution from the twin fault model. https://rokuwaki.github.io/geol/tmp/2024_royyamyf_eartharxiv_movieS1.mp4

**Movie S2.** Snapshots of the potency-rate density tensor distribution from the single fault model. https://rokuwaki.github.io/geol/tmp/2024_royyamyf_eartharxiv_movieS2.mp4